Coherence in macroscopic high harmonic generation for spatial focal phase distributions of monochromatic and broadband Gaussian laser pulses

B. GHOMASHI,[1,2] R. REIFF,[1,2] AND A. BECKER[1,*]

[1] *JILA and Department of Physics, University of Colorado, Boulder, Colorado 80209-0440, USA*
[2] *These authors contributed equally*
[*] *andreas.becker@colorado.edu*

Abstract: Efficient application of ultrafast laser sources from high harmonic generation requires an understanding of how the spectrum can be controlled – the extent of the highest harmonics and the strength and cleanness of the harmonic lines. We study one important aspect in the coherent build-up of macroscopic high-order harmonic generation, namely the impact of different phase distributions in the focal area on the features of the generated radiation. Specifically, we compare the high harmonic signals for the commonly-used Gouy distribution of a monochromatic beam with those for the phase distribution of a short broadband Gaussian pulse. To this end, we apply a theoretical model in which the microscopic yields are obtained via interpolation of results of the time-dependent Schrödinger equation, which are then used in an individual-emitter approach to determine the macroscopic signals. Regions of poor and good coherent build-up as a function of the position of the gas jet are identified using measures for the strength of the harmonic lines and for the impact of off-harmonic radiation. While the largest extent of the spectra as well as the strongest contribution of off-harmonic radiation is found for positioning the gas jet after the focus for both distributions, the relative strength of the harmonics is overall weaker for the short Gaussian pulse distribution and the spectra differ for a gas jet positioned at the focus. These differences are mainly caused by the additional dependence of the focal phase in the transverse direction for the short Gaussian pulse distribution.

1. Introduction

High harmonic generation (HHG) is a non-perturbative and highly nonlinear frequency conversion process, which occurs when an intense laser pulse interacts with a gaseous, liquid or solid medium [1,2]. For bright harmonic emission, it is required that the electric field strength of the generating laser pulse be comparable to that of the Coulomb field inside the microscopic target and that conditions for a coherent build-up of the radiation inside the macroscopic medium are present (for reviews, see [3–6]). The harmonics are emitted at multiples of the driving laser frequency with wavelengths ranging from the ultraviolet [7] to the soft x-ray regime [8]. The polarization of the harmonics can be controlled from linear to elliptical to circular [9–11] and structured harmonic light beams with time-varying orbital angular momentum have been demonstrated [12,13]. In view of these properties, HHG has become an important compact laser light source with many applications in ultrashort pulse generation, time-resolved imaging of nuclear and electronic dynamics, and imaging with high spatial resolution (for reviews, see [4,5,14–29]). To make efficient use of HHG sources, it is important to understand both the harmonic generation process at the microscopic single-atom level as well as the coherent build-up of harmonic radiation from the many atomic emitters in the laser focus.

At the microscopic level the HHG spectrum results from the dipole acceleration of an electron, initially bound inside the target atom (molecule, solid), interacting with the strong external field.

The physical mechanism is well described by the three-step model [30–32]. According to this model, the electric field of the intense laser pulse suppresses the Coulomb barrier of the most weakly-bound electrons in the target. This permits tunneling of an electron wave packet, which then propagates in the oscillating electric field. Depending on the time of release, the wave packet can be steered back to the parent ion and, with some probability, recombine with the parent ion under emission of a high-energy photon. In the semiclassical approach of HHG [32], the wave packet returns via two classes of trajectories distinguished by their excursion time in the continuum, named the short and long trajectories.

The high peak intensities necessary to drive the microscopic HHG process can be generated by focusing a short laser pulse into an atomic gas medium. It is challenging to achieve a coherent build-up of the HHG signals from the many atoms in the generating medium since the process depends on several aspects [5,33,34]. One of these aspects is the spatial phase distribution of the driving laser pulse in the focus, which results in a spatially-dependent carrier-envelope phase (CEP). Usually, a π-phase shift across the focus – also commonly known as Gouy phase [35] – is taken into account for the analysis of the coherent build-up of the HHG signal. However, this phase distribution corresponds to that of a monochromatic Gaussian beam. Focused short Gaussian pulses with a broad frequency spectrum, which are often used in a HHG experiment, have a different spatial phase dependence [36,37]. The difference to the Gouy phase is given by an additional focal phase term which scales with the so-called Porras factor g_0 that is determined by the specific laser system. This second term introduces a variation of the phase transverse to the propagation direction which is not present in the Gouy phase and depends on g_0 and the distance from the focus along the propagation direction. The impact of the focal phase distribution on short-pulse induced strong-field processes has only recently been studied for few strong-field observations, namely electron backscattering at nanoscale metal tips [38], photoelectron spectra in few-cycle laser pulses [39], and the angular distributions of low-order harmonics [40]. The perspective to use HHG sources for spectroscopic and other applications require developing understanding of how different spatial focal phase distributions affect the extent of the spectrum to highest harmonic number, the strength and cleanness of harmonic lines, as well as the often unwanted occurrence of radiation at off-harmonic frequencies. The goal of the present work is to show that consideration of the phase distribution of a broadband Gaussian pulse makes a marked difference on the coherent build-up of the macroscopic HHG signal as compared to the case of the previously considered Gouy distribution. As a consequence, the features of the generated harmonic radiation depend on the positioning of the gas jet with respect to the laser focus differently for the two phase distributions.

In our theoretical study we compare the coherence (or, phase matching) of high harmonic emission in a macroscopic atomic gas jet for spatial focal phase distributions of the driving laser pulse with and without the additional focal phase term for the focused short Gaussian laser pulse. We focus on situations with a negative Porras factor of $g_0 = -2$ which has been reported in a recent experiment [38]. The comparison is based on the analysis of macroscopic harmonic signals that are calculated as the superposition of the fields generated by individual emitters in the focus [40,41]. This approximation applies for a thin medium or low gas density regime and small ionization probability for which the generated radiation does not interact with the medium. The harmonic signal generated by each of the emitters is determined by applying an interpolation technique to make use of ab-initio solutions of the time-dependent Schrödinger equation (TDSE) [40,42].

The article is organized as follows: In section 2, we present the theoretical methods applied to calculate the microscopic and macroscopic high-order harmonic response. This includes a brief outline of the techniques used to solve the time-dependent Schrödinger equation, the interpolation method, and the individual-emitter approach used to determine the macroscopic signal. Furthermore, we discuss the differences in the phase distribution with and without

consideration of the phase arising for a short broadband Gaussian pulse. We then present in section 3 our findings for the coherent build-up of macroscopic radiation for the two phase distributions considered. First, we introduce measures for the strength of the harmonic line and the impact of off-harmonic radiation along with a discussion of the general features of the harmonic signal. Regions of good phase matching are next identified and discussed based on an analysis using the different phase distributions. The article ends with a brief summary.

2. Theory

A full description of the HHG process requires the coupled solution of Maxwell's equations at the macroscopic level and of the time-dependent Schrödinger equation (TDSE) for each of the atomic emitters at the microscopic level. Such an approach however requires formidable computer resources due to the large number of atoms in the medium, for which the TDSE needs to be solved (see [3,43,44] for further discussion). In this work we therefore apply an approximation method [40,42] in which the macroscopic harmonic yield is determined as a superposition of fields of point-like emitters using ab-initio TDSE results at the single-atom level. To keep the overall simulation efficient, interpolation of TDSE results across intensity and carrier-envelope phase is used. Next, we briefly discuss the methods to interpolate the TDSE results and then review the macroscopic simulation for both Gouy and short Gaussian pulse phase distributions.

2.1. Microscopic TDSE calculations

We obtain ab-initio microscopic HHG spectra by solving the TDSE with the Hamiltonian (Hartree atomic units are used: $e = \hbar = m = 1$ a.u.):

$$H(t) = -\frac{1}{2}\nabla^2 - \frac{1}{r} + \mathbf{r} \cdot \mathbf{E}(t),\tag{1}$$

where $\mathbf{E}(t)$ is the electric field. In all calculations, the initial state was set to be the ground state of the hydrogen atom potential. The laser field has been taken to be linearly polarized in the y-direction. To ensure the electric field integrates to zero, we set the vector potential

$$A(t) = A_0 \sin^2\left(\frac{\pi t}{\tau}\right) \sin(\omega(t - \tau/2))\tag{2}$$

where $A_0 = \frac{c\sqrt{I}}{\omega}$, and $\tau = \frac{2\pi N}{\omega}$ and c is the speed of light, I is the peak intensity, and N is the number of cycles in the pulse. The electric field is obtained as $E_y(t) = -\frac{1}{c}\frac{\partial}{\partial t}A(t)$. We note that Eqs. (1) and (2) refer to the microscopic description of the process. Macroscopically, the intensity and, hence, the amplitudes of the vector potential and the electric field depend on the location in the focal area. The spatial dependence of the carrier-envelope phase for monochromatic and short Gaussian laser pulses will be introduced and discussed in Sec. 2.3.

To solve the TDSE, we have expanded the wavefunction in 30 spherical harmonics and discretized the radial part of the wavefunction and the potential utilizing fourth order finite difference on a radial grid with spacing $dr = 0.2$ a.u. and grid sizes up to $r_{max} = 100$ a.u. The Crank-Nicolson method has been applied to propagate the wavefunction starting from the initial state. As absorbing boundary, we have used exterior complex scaling, where the edge of the grid (10%) is rotated into complex space by an angle $\eta = \pi/4$. The HHG spectra have been obtained by evaluating the dipole acceleration $a(t)$ using the Ehrenfest theorem

$$a(t) = \left\langle -\frac{\partial}{\partial z}\left(-\frac{1}{r}\right) \right\rangle.\tag{3}$$

The harmonic response is then given by taking the Fourier transform of the dipole acceleration,

$$a(\omega) = \int_0^T a(t)e^{-i\omega t}dt,\tag{4}$$

and the harmonic spectrum $P(\omega) = |a(\omega)|^2$.

2.2. Macroscopic model calculations

To determine the macroscopic radiation signal at a far-field detector, we consider the following arrangement [40,42]: The driving linearly polarized laser propagates in the $\hat{\mathbf{Z}} = \hat{\mathbf{z}}$ direction and the polarization direction is in the $\hat{\mathbf{Y}} = \hat{\mathbf{y}}$ direction. We denote macroscopic (microscopic) coordinates with upper (lower) case letters. Only harmonic radiation polarized along $\hat{\mathbf{Y}}$ is being considered. We follow the individual-emitter approach used in [41]. The macroscopic yield is obtained as the superposition of fields generated at different points in the medium. The spectral distribution of the total radiation is then generated by atoms located at $\mathbf{R}_j$ ($j = 1, 2, 3, \ldots$) as:

$$\mathbf{E}(\mathbf{R}_d, \omega) = \frac{1}{c^2 |\mathbf{R}_d|} e^{-i\frac{\omega}{c}|\mathbf{R}_d|} \sum_j a_j(\omega) e^{-i\frac{\omega}{c}[\mathbf{R}_j \cdot (\hat{R}_d - \hat{Z})]} \hat{\mathbf{Y}} , \qquad (5)$$

where $a_j(\omega)$ is the TDSE result for the microscopic dipole acceleration in frequency domain. We further consider the delay of the driving laser reaching the radiator, $(\mathbf{R}_j \cdot \hat{\mathbf{Z}})/c$, by adding the corresponding additional phase. In the calculation it has been assumed that the relative location of the detector, $\mathbf{R}_d$, is far away from the individual atoms. This leads to the following approximations: $|\mathbf{R}_j| \ll |\mathbf{R}_d|$ and, hence, $|\mathbf{R}_d - \mathbf{R}_j| \approx |\mathbf{R}_d| - \mathbf{R}_j \cdot \hat{\mathbf{R}}_d$ and $\frac{1}{|\mathbf{R}_d - \mathbf{R}_j|} \approx \frac{1}{|\mathbf{R}_d|}$. In the present work we have considered macroscopic results for on-axis harmonic radiation only, i.e. $\hat{\mathbf{R}}_d = \hat{\mathbf{Z}}$, which simplifies Eq. (5) significantly. The prefactor in Eq. (5) universally scales the results; it is therefore dropped from the computations.

This approximation to the full Maxwell solution applies for the thin medium or low gas density regimes. Furthermore, the approach does not account for any phase mismatch due to the presence of free electrons. Therefore, in practice it is applicable at intensities low enough so that free electron dispersion does not play a significant role. Other effects, e.g., a curving of the wavefront, are also not present in the approach. In a typical high-harmonic gas jet experiment, even at low-pressure densities, the number of atoms is of the order of 10^{12} or larger, with random sampling of Eq. (5) converging on the scale of 10^4 or more emitters [42]. Obtaining TDSE results of the microscopic harmonic response for such a large number of atoms is only feasible with substantial computation resources. As an alternative we have applied an interpolation technique [40,42] in which the complex spectrum $a(\omega)$ is numerically calculated for a set of peak intensities over a desired sampling range. For a given point in frequency, the complex spectrum is interpolated across intensities using cubic splines with not-a-knot end conditions. The impact of the end conditions is minimized by ensuring that relevant intensities are well-contained within the sampling range. The full complex spectrum is then reconstructed from these slices. The applicability of the interpolation technique has been verified in previous work [40,42].

In addition to the variation of the peak intensity across the focal volume, the effects of the carrier-envelope phase (CEP), ϕ, have to be considered for the macroscopic harmonic yields. In few-cycle pulses CEP impacts the microscopic harmonic generation, while for pulses as considered in this work the impact on the microscopic signal is negligible [42]. However, the spectral phase effects and the focal phase distribution cannot be discounted in macroscopic summation, which is a focus of the present work. The spectral phase can be approximated by [41]:

$$\Phi(\omega, \phi) = \Phi(\omega, \phi = 0) + \phi H(\omega) , \qquad (6)$$

where $H(\omega)$ is the harmonic number rounded to the nearest odd integer. Previously, we have shown that in the parameter regime considered below exact TDSE results agree well with the above approximation, which we have therefore used in the macroscopic calculations [40,42].

For the atomic gas jet we have considered hydrogen atoms distributed in a cylinder with a Gaussian distribution aligned perpendicular to the laser propagation. In the calculations the position of the center of the gas jet is varied along the laser propagation direction Z. To obtain the macroscopic HHG signal we use Monte Carlo sampling of the locations of the atoms, discarding

locations where the intensity is below a given cut-off (here, $I(\mathbf{R}_j)<0.032I_0$) as the corresponding generated radiation does not contribute significantly to the total radiation.

2.3. Focal phase distribution

The spatial phase distribution for a short broadband Gaussian laser pulse has been derived by Porras and co-workers as [36,37]:

$$\Delta\Phi_F(Z,R) = -\arctan\left(\frac{Z}{Z_R}\right) + g_0 \frac{\left[1 - 2\left(\frac{R}{w(Z)}\right)^2\right]}{\frac{Z}{Z_R} + \frac{Z_R}{Z}} \tag{7}$$

with the Porras factor

$$g_0 = \left.\frac{dZ_R(\omega)}{d\omega}\right|_{\omega_0} \frac{\omega_0}{Z_R(\omega_0)} \tag{8}$$

and the frequency-dependent Rayleigh range

$$Z_R(\omega) = \frac{\omega W^2(\omega)}{2c} . \tag{9}$$

In Eq. (7), Z and R are the positions along and transverse to the propagation of the laser, ω_0 is the central frequency of the laser, $w(Z) = W_0\sqrt{1 + (\frac{Z}{Z_R})^2}$ is the beam radius of the center frequency, where $Z_R \equiv Z_R(\omega_0)$. Furthermore, $W(\omega)$ is the frequency-dependent input waist, $W_0 = W(\omega_0)$ is the central frequency beam waist at the focus and c is the speed of light. The spatially-dependent phase determines the evolution of the CEP across the focal area and, hence, the spectral phase of the harmonics via Eq. (6).

The first term in Eq. (7) is the Gouy phase for monochromatic beams which gives a longitudinal phase dependence along the laser propagation direction, while in the transverse direction the Gouy phase is constant. The second term scales with the Porras factor g_0 and describes the difference to the Gouy phase for beams with a frequency bandwidth. For a negative value of $g_0 = -2$, which has been considered in strong-field experiments and theory so far [38–40,42] and will be used here as well, the focal phase term has the same sign as the Gouy phase on-axis. However, it introduces a dependence in the transversal direction, and changes sign at certain radial distances, which depend on g_0 and Z. We may therefore expect that, besides potential other effects, transversal phase matching of high harmonics for spatial phase distributions with and without the second (ultrashort) focal phase term in Eq. (7) is different. It has recently been shown [45,46] that such phase matching in the transverse direction can play a significant role, besides the generally considered longitudinal phase matching in high harmonic generation.

3. Results and discussion

3.1. Features and measures

In order to study the signatures in the high harmonic signals for different gas jet positions for the cases of a Gouy and the short Gaussian pulse phase spatial distribution, we first provide an overview and introduce some measures which are useful for the further analysis. In our study we have considered HHG induced by an intense 20-cycle laser pulse at a central wavelength of 800 nm and a peak intensity of 1.2×10^{14} W/cm^2 during the interaction with atomic hydrogen. The spatial profile of the laser is chosen to be a Gaussian beam with a beam waist of 30 μm ($Z_R \approx 3500$ μm). We did not consider fluctuations in intensity and phase of the laser, which may occur over the focal area and/or shot-by-shot in an experiment. We therefore focus on general qualitative conclusions from the present results only. Two hundred fifty microscopic TDSE

calculations were performed at intensities in the range from 1.0×10^{12} W/cm^2 to 2.5×10^{14} W/cm^2 in steps of 10^{12} W/cm^2. The density was modeled as a Gaussian distribution of width $\sigma = 800$ μm and a peak density of 10^{18} cm^{-3}. Fluctuations of the gas density are not taken into account in the present study, in which we focus on some basic qualitative differences in phase matching for the two phase distributions.

In Fig. 1 we compare the macroscopic HHG signals (vertical axis) as a function of the gas jet position (horizontal axis) for (a) the Gouy and (b) the short Gaussian pulse phase distribution (with Porras factor $g_0 = -2$). Each spectrum is scaled such that the strength of the fundamental is equal to 1. The comparison reveals some obvious similarities and differences. First, it has been reported in earlier theoretical studies based on the Gouy spatial phase distribution that the largest extension of the harmonic spectrum is typically found for positions of the gas jet after the laser focus [41]. Our results not only confirm this feature but also show that the same observation holds for the results obtained for the short Gaussian pulse phase distribution. Another feature that occurs in a similar way in both spectra is the importance of off-harmonic radiation in the spectra. In both spectra we observe strong contributions at off-harmonic frequencies when the gas jet is positioned in a certain region after the laser focus.
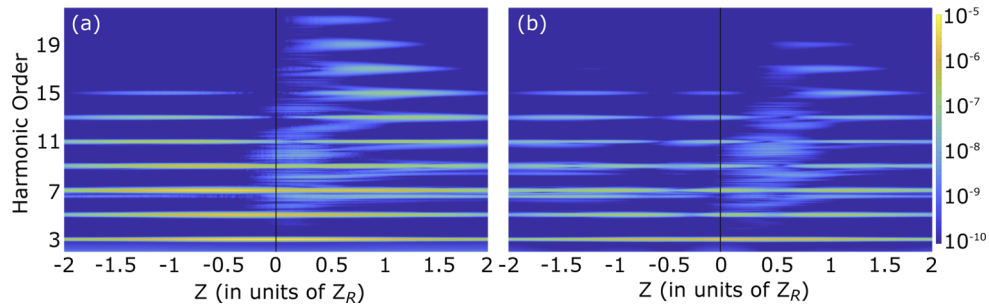

Fig. 1. Comparison of high harmonic radiation spectra as a function of the position of the gas jet along the propagation direction of the driving laser obtained using (a) the Gouy ($g_0 = 0$) and (b) a short Gaussian pulse phase distribution ($g_0 = -2$). Note that the propagation distance is scaled in units of the Rayleigh length $Z_R = Z_R(\omega_0)$. Laser parameters: Peak intensity $I_0 = 1.2 \times 10^{14}$ W/cm^2, Porras factor $g_0 = -2$, central frequency waist at focus $W_0 = 30$ μm, Rayleigh length $Z_R = 3534$ μm. Gas jet parameters: Gaussian distribution of width $\sigma = 800$ μm, peak gas density of 1×10^{18} cm^{-3}. The vertical black line at $Z = 0$ is drawn to guide the eye.

On the other hand, the relative strength of the harmonics is apparently different in the two spectra in Fig. 1. For the short Gaussian pulse distribution the maximum harmonic strengths are weaker than those obtained for the Gouy distribution. Another difference in the two spectra is the relative strength of each harmonic as a function of the position of the gas jet. This can be best seen in the higher harmonics. For example in the case of the Gouy distribution, the harmonic strength is minimum when the gas jet is near the laser focus. In contrast, for the short Gaussian pulse distribution the results show a local maximum for $Z \approx 0$, while there are two minima for the gas jet position either before or after the focus.

In order to study the strength of the harmonics and the relevance of the off-harmonic radiation, we use the following measures. Their application is illustrated using the example of the 9th harmonic for the short Gaussian pulse phase distribution in Fig. 2. To investigate the strength of the harmonic signal we have considered both the signal at the harmonic line itself as well as the integrated signal over a small region around the harmonic, i.e. $\int_{(N-\delta)\omega}^{(N+\delta)\omega} S(\Omega)d\Omega$, where $S(\Omega)$ is the macroscopic radiation signal and we have chosen $\delta = 0.25$ in our analysis. As can be seen from the comparison in Fig. 2(b) both measures reflect the strength of the 9th harmonic as a

function of gas jet position, including the locations of maxima and minima. In the remainder of our analysis we will use the integrated signal as a measure for the strength of the harmonic.
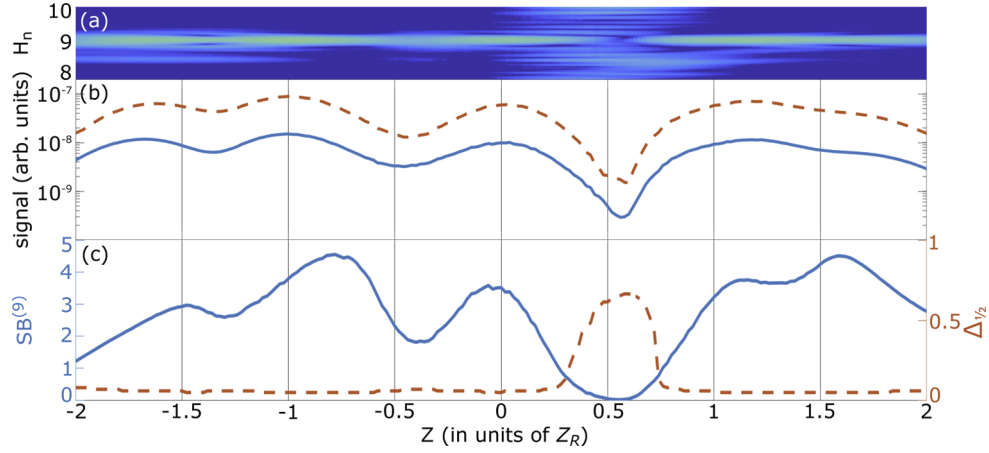

Fig. 2. (a) Radiation spectrum for short Gaussian pulse phase distribution ($g_0 = -2$) around 9th harmonic as a function of gas jet position (signal scaling as in Fig. 1). (b) Signal $S(\omega)$ at harmonic (dashed line) and integrated signal $\int_{(N-\delta)\omega}^{(N+\delta)\omega} S(\Omega)d\Omega$ (solid line). (c) Half-width $\Delta_{1/2}^{(9)}$ (dashed line) and sideband measure $SB^{(9)}$ (solid line) of harmonic. Laser and gas jet parameters as in Fig. 1.

To examine the narrowness of the Nth harmonic line and the role of off-harmonic radiation around the Nth harmonic, we define a half-width $\Delta_{1/2}^{(N)}$ via:

$$\frac{\int_{(N-\Delta_{1/2}^{(N)})\omega}^{(N+\Delta_{1/2}^{(N)})\omega} S(\Omega)d\Omega}{\int_{(N-1)\omega}^{(N+1)\omega} S(\Omega)d\Omega} = \frac{1}{2} \; . \tag{10}$$

If $\Delta_{1/2}^{(N)}$ is small (large) the Nth harmonic line is narrow (broad). We further utilize a sideband measure defined as:

$$SB^{(N)} = \frac{\int_{(N-\delta)\omega}^{(N+\delta)\omega} S(\Omega)d\Omega}{\int_{(N-1)\omega}^{(N+1)\omega} S(\Omega)d\Omega - \int_{(N-\delta)\omega}^{(N+\delta)\omega} S(\Omega)d\Omega} \tag{11}$$

with $\delta = 0.1$. For larger (smaller) $SB^{(N)}$, the radiation is more concentrated at (off) the Nth harmonic line. If $SB^{(N)}<1$, the radiation at the Nth harmonic line is suppressed as compared to the off-harmonic radiation. The results in Fig. 2(c) indeed show that the minima in $SB^{(9)}$ (solid line) coincide with the regions of significant off-harmonic radiation in Fig. 2(a). Especially, the region of suppressed radiation at the 9th harmonic correlates with values below 1 for $SB^{(9)}$ and a strong maximum in $\Delta_{1/2}^{(9)}$ (dashed line). While the dependence of the two curves on Z are similar in Fig. 2(c), variations between extrema in the half-width measure is much smaller and hardly visible. Therefore, we decided to use the sideband measure $SB^{(N)}$ for the analysis below.

3.2.   *Strength of harmonics and extension of spectrum*

In Fig. 3 we present the integrated signal strength of three harmonics in different regions of the spectrum – below-threshold (7th harmonic, solid lines), plateau (13th harmonic, dashed line) and near the cut-off (19th harmonic, dashed-dotted line) – as a function of the position of

the gas jet obtained for (a) the Gouy phase distribution and (b) the short Gaussian pulse phase distribution. The data provide a quantitative measure of the qualitative observations made in the discussion of the results in Fig. 1. For the Gouy distribution the strongest below-threshold harmonics are obtained for a gas jet position before the focus. In contrast and in agreement with earlier observations [41], the optimum position is after the focus for harmonics above the ionization threshold. This is most striking for the extension of the spectrum to the highest harmonics. While for the highest harmonics the same observation holds with a short Gaussian pulse distribution, the results for the lower harmonics in that case differ from those obtained for the Gouy distribution. For below-threshold and plateau harmonics we find that there are three positions – one before, one near, and one after the focus – at which the respective harmonic signal is strong. Most distinctive is the difference between the occurrence of a maximum (short Gaussian pulse distribution) and a minimum (Gouy distribution) for the generation of plateau harmonics (c.f., 13th harmonic in Fig. 3) for the gas jet position near the focus.
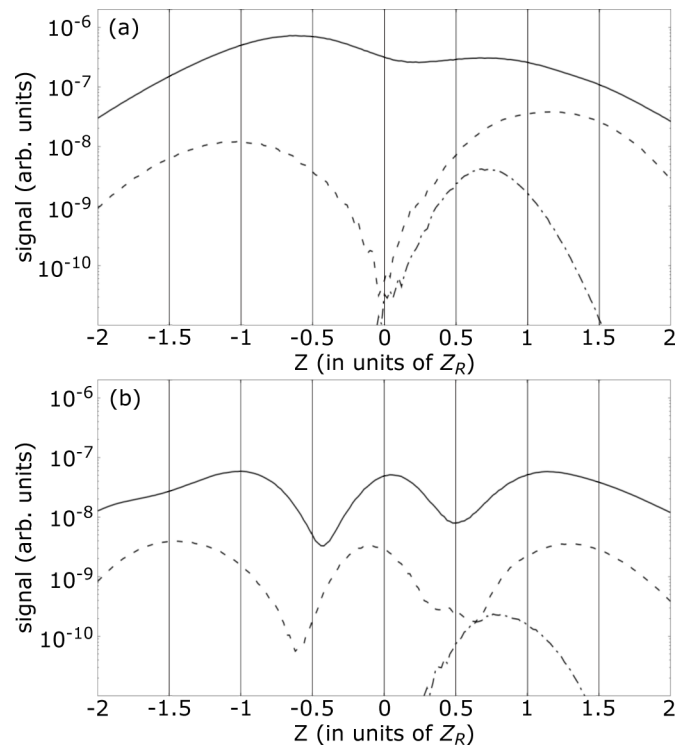

Fig. 3. Integrated signal strength as a function of the gas jet position for 7th (solid lines), 13th (dashed lines), and 19th (dot-dashed lines) harmonics obtained using (a) the Gouy and (b) the short Gaussian pulse phase distribution. Laser and gas jet parameters as in Fig. 1.

For a strong signal, radiation emitted from many atoms must interfere constructively. It is therefore expected that the strongest harmonic signal is found from regions in which the variation of the total phase is small [41]. In our calculations the total phase consists of two contributions: On the one hand the intrinsic phase of the harmonics, which results from the microscopic rescattering process and depends on the intensity of the laser and the harmonic number. The second contribution is either the Gouy or the short Gaussian pulse phase (c.f., Eq. (7)). To obtain insights into the results for the harmonic radiation, we therefore compare distributions of the individual contributions and of the total phases along and transverse to the propagation direction for the different harmonics in Fig. 4.
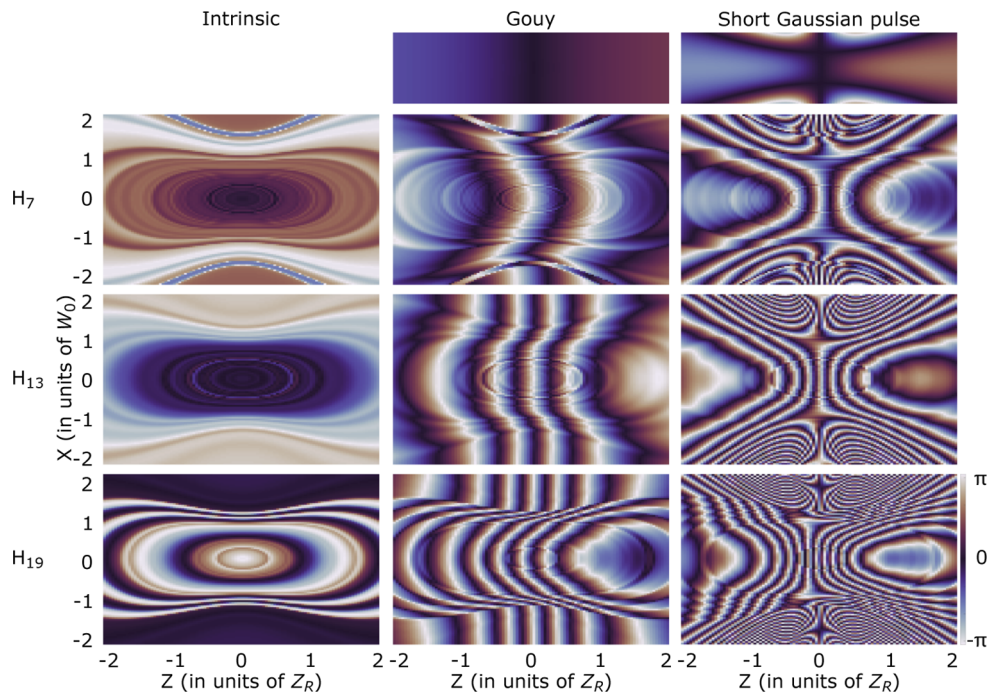
Fig. 4. Comparison of intrinsic (left), Gouy+intrinsic (middle) and short Gaussian pulse+intrinsic (right) phase distributions for 7th (second row), 13th (third row), and 19th (bottom row) harmonic. Top row shows the Gouy and short Gaussian pulse phase distributions (c.f., Eq. (7). Laser and gas jet parameters as in Fig. 1.

In the top row, the Gouy ($g_0 = 0$) and short Gaussian pulse ($g_0 = -2$) phase distributions (c.f. Eq. (7)) are shown. In the other rows we present the intrinsic phase of each of the three harmonics (left column), and the total phases for the two cases, i.e. Gouy phase + intrinsic phase (middle) and short Gaussian pulse phase + intrinsic phase (right). Since the intrinsic phase depends on the intensity of the laser pulse only, the corresponding distributions are symmetric with respect to the two axes $Z = 0$ and $X = 0$. The intrinsic phase increases along the Z-axis for $Z<0$ and decreases for $Z>0$. The variation of the phase depends for each of the harmonics on the intensity gradient. It is therefore smallest near the focus and in the tails of the distribution. On the other hand, the intrinsic phase varies fastest near the inflection point of the Gaussian intensity distributions. Furthermore, we note that the variation of the intrinsic phase at a given point in the focal area depends on the harmonic number. In contrast to the intrinsic phase, the other individual contributions – namely the Gouy and short Gaussian pulse phase distribution – are not symmetric with respect to $Z = 0$. Instead, both decrease along the Z-axis for $X = 0$. We note that the gradient of decrease is stronger for the short Gaussian pulse phase. Additionally, as mentioned before, the Gouy phase is constant in the transverse direction at a given Z, while there is a dependence in this direction for the short Gaussian pulse distribution.

We now turn to the total phases, i.e. Gouy + intrinsic phase and short Gaussian pulse + intrinsic phase. Since the intrinsic phase is symmetric across $Z = 0$ but the other two distributions are not symmetric, the two total distributions also do not exhibit a symmetry with respect to $Z = 0$. As mentioned above, for the strength of the corresponding harmonics it is most interesting to identify regions in which the variation of the total phase is small. In these regions there can be sequences of increases and decreases in the total phase distributions. But, overall the phase distributions are continuous and smooth as function of the spatial parameters. Any visual

impression of discontinuities in Fig. 4 or one of the following figures is due to the discrete sampling of locations in the numerical calculations and/or the color coding.

For the lowest harmonic and the Gouy distribution (2nd row, middle panel) there are two regions – one before (around $Z = -0.5$) and one after the focus (close to $Z = 1$) – in which the total phase varies rather slowly, leading to favorable conditions for a coherent build-up of signal. Correspondingly, there are two maxima in the strength of the 7th harmonic (solid line in Fig. 3(a)). Within the area of slowly varying phase the maxima occur for positions closest to the focus, since those correspond to the highest intensity. The maximum strength is slightly larger before the focus, which is likely due to the fact that for $Z<0$ the area of slowly varying phase starts at smaller absolute distance to the focus, and hence at somewhat higher intensities. Since the intrinsic phase of the higher harmonics varies more quickly, the curvature of the lines of equal total phase for the Gouy distribution over part of the region with $Z<0$ changes for the 13th and 19th harmonics as compared to the case of the below-threshold harmonic. Consequently, the largest area of slow variation in the total (Gouy + intrinsic) phase and the strongest signal for the higher harmonics is found for positions of the gas jet after the focus (Fig. 3(a)). This result and the interpretation of the coherence conditions for the two higher harmonics in a Gouy phase distribution agree with that made in an earlier work [41].

As already mentioned above the short Gaussian pulse distribution differs from the Gouy distribution in two aspects (c.f., two panels in the top row of Fig. 4). First, the short Gaussian pulse phase varies in the transverse direction, while the Gouy phase is constant in that direction. This restricts the areas of slowly varying total (short Gaussian pulse + intrinsic) phase in the transverse direction. Consequently, there is less efficient phase matching in the transverse direction as compared to the total phase distribution for the Gouy phase, which explains the overall observation of weaker harmonics for the short Gaussian pulse distribution. Further indication of this transversal phase matching effect can be seen from the comparison of the results in Fig. 5. The area over which the total phase of the 7th harmonic changes by less than $\pi/2$ at the position of maximum signal strength is clearly smaller in the transverse direction for the short Gaussian pulse distribution (Fig. 4(b)) than for the Gouy distribution (Fig. 4(a)). We further observe that in the case of the short Gaussian pulse distribution the least efficient coherent signal build-up of the two lower harmonics (c.f., Fig. 3(b) solid and dashed lines) occurs at positions at which the total phase is varying most quickly in the transverse direction (c.f., right column in Fig. 4). The importance of transverse phase matching has been emphasized previously [45,46].
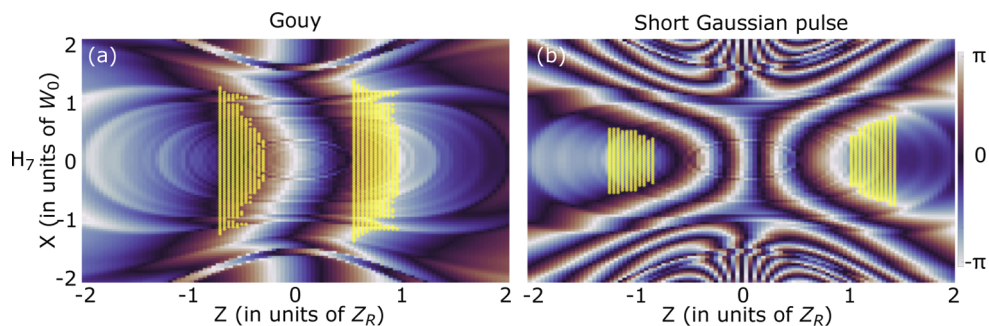

Fig. 5. Comparison of areas over which the total phase changes by less than $\pi/2$ with respect to the central point in the gas jet: (a) 7th harmonic, Gouy phase distribution and (b) 7th harmonic, short Gaussian pulse phase distribution. Considered are gas jet positions before and after the focus at which the strength of the harmonic signal is at maximum (c.f., Fig. 3). Note that the areas are restricted along the propagation direction by the width of the gas jet. Laser and gas jet parameters as in Fig. 1.

The second difference in the two phase distributions is that the longitudinal phase variation is stronger in the short Gaussian pulse distribution. As a result, the two areas of slowly varying total phase remain present for all harmonics for the short Gaussian pulse + intrinsic phase distribution (c.f., right column in Fig. 4). However, the more rapidly-changing intrinsic phase at higher harmonics causes the area to be moved farther away from the focus for positions $Z<0$. This results in the suppression of harmonic strength for the cut-off harmonic before the focus (c.f., Fig. 3(b), dashed-dotted line) for the short Gaussian pulse distribution.

We finally consider the difference in strength near the focus for the 13th harmonic. Based on the results in the third row of Fig. 4, our interpretation of the minimum in strength for the Gouy distribution is related to the observation that near the focus the total phase varies most quickly in the longitudinal direction leading to poor phase matching conditions. Regarding the longitudinal direction similar quick variation can be observed in case of the short Gaussian pulse distribution. However, the extension of the area with similar total phase is rather large near the focus which likely explains the formation of a maximum in harmonic signal near the focus. We may note that the phase variation at $Z = 0$ also leads to interference effects in the angular distribution of the below-threshold harmonics for the short Gaussian pulse distribution [40].

3.3. Narrowness of harmonics and off-harmonic radiation

In this section we investigate the relevance of off-harmonic radiation as compared to the nearest harmonic line. As an example for our study we consider the 11th harmonic and present in Fig. 6 the sideband measure $SB^{(11)}$ for both spatial phase distributions. Large values of $SB^{(11)}$ indicate that the radiation off the harmonic line is much less intense that the 11th harmonic radiation. At the respective gas jet positions the harmonic line is narrow, which shows that the line can be well used for spectroscopic applications when filtered appropriately. In contrast, low values of $SB^{(11)}$ indicate regions at which there occurs significant off-harmonic radiation and the harmonic line itself may even be suppressed. The comparison in Fig. 6 shows for the short Gaussian pulse distribution two regions with strong off-harmonic radiation around $Z = \pm 0.5 Z_R$, while off-harmonic radiation is most relevant close to the focus for the Gouy distribution.
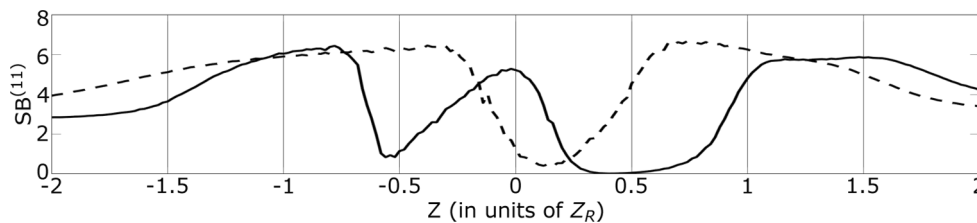

Fig. 6. Comparison of sideband measure $SB^{(11)}$ for the 11th harmonic as a function of the position of the gas jet for Gouy (dashed line) and short Gaussian pulse (solid line) phase distributions. Laser and gas jet parameters as in Fig. 1.

To understand the results in terms of macroscopic coherent build-up of radiation we consider the phase distributions for radiations emitted at frequencies below ($\Omega = 10.5\omega$), at ($\Omega = 11\omega$) and above ($\Omega = 11.5\omega$) the 11th harmonic, presented in Fig. 7. As expected, the intrinsic phase of the off-harmonic radiation varies much more rapidly than that of the 11th harmonic as a function of intensity in the focal area (left column). The regions of slowest variation in the intrinsic phase for the off-harmonic radiation are near the focus and yield similar regions just after the focus for the Gouy (middle column) and at about $Z = 0.5 Z_R$ for the short Gaussian pulse distribution (right column). These regions indeed correspond to minima in the respective distributions for $SB^{(11)}$ in Fig. 6. Moreover, for the short Gaussian pulse distribution the low-variation region for gas jet positions after the focus is larger for the radiation at the frequency below the harmonic, which

coincides with the qualitative observation that the off-harmonic radiation is more relevant at these frequencies than those above the 11th harmonics (c.f., Fig. 1(b)). The explanation for the second minimum in the sideband measure before the focus in case of the short Gaussian distribution is different. Here, the measure primarily indicates the suppression of the harmonic line itself, as one can see qualitatively in Fig. 1(b), while off-harmonic radiation remains relative insignificant as well. Correspondingly, we observe in the phase distributions for all three frequencies in Fig. 7 (right column) a fast variation of the total phase for gas jet positions in this region. This clearly indicates overall poor phase matching conditions for frequencies at and around the 11th harmonic for the short Gaussian pulse distribution, if the gas jet is positioned in this region before the focus.
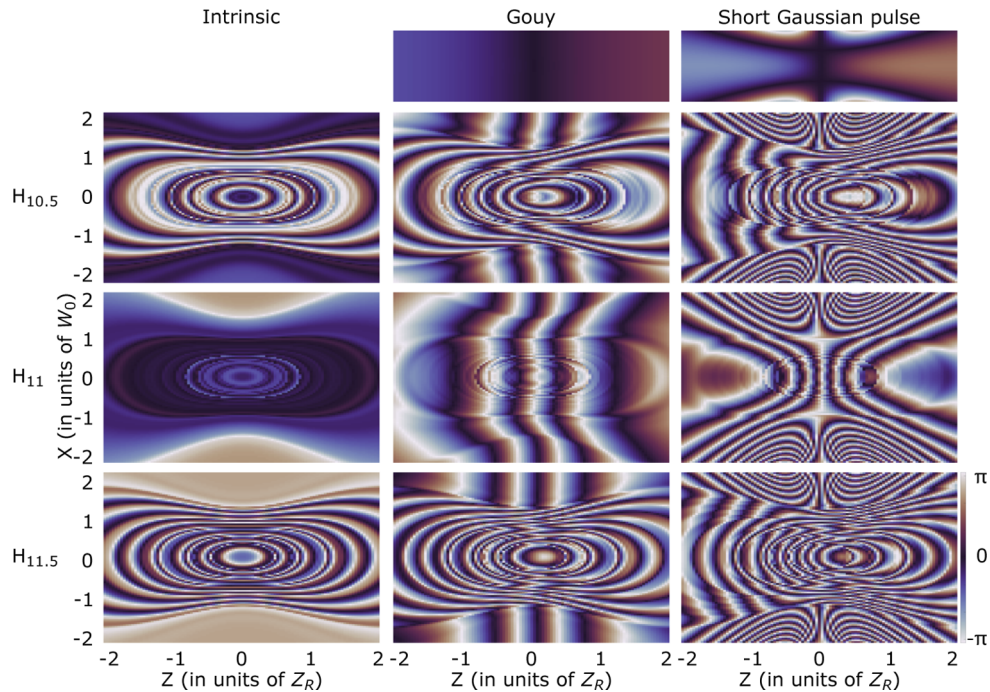

Fig. 7. Comparison of intrinsic (left), Gouy+intrinsic (middle) and short Gaussian pulse+intrinsic (right) phase distributions for radiation at frequencies below (10.5ω, termed $H_{10.5}$, second row), at (11ω, termed H_{11}, third row) and above (11.5ω, termed $H_{11.5}$, third row) the 11th harmonic. Top row shows the Gouy and short Gaussian pulse phase distributions (c.f., Eq. (7)). Laser and gas jet parameters as in Fig. 1.

4. Summary and concluding remarks

In summary, similarities and differences in the coherent build-up of macroscopic high harmonic generation signals for different phase distributions in the focal area have been studied. The investigation is based on numerical data from a theoretical model, in which yields obtained from the time-dependent Schrödinger equation are interpolated and then used in an individual-emitter approach to obtain the macroscopic signals. Results assuming the Gouy phase distribution for a monochromatic beam are compared with those resulting from the phase distribution for a short broadband Gaussian pulse as a function of the position of the atomic gas jet. In both cases the largest extent of the spectra – hence, the highest harmonics – are generated for a gas jet position somewhat after the laser focus. In the same region we however also find – in both sets of spectra – significantly more off-harmonic radiation than in cases when the gas jet is positioned before the

focus. Both features can be explained via regions of slowly varying total phase which occur for both the Gouy and the short Gaussian pulse distribution for the harmonic and the off-harmonic radiation at similar gas jet positions after the focus. On the other hand, we observe that, in general, the harmonic signals are considerably weaker for the short Gaussian pulse distribution. This is caused by the additional dependence of the phase in the transverse direction which only occurs for the short Gaussian pulse distribution. As a consequence, the areas of slowly varying phase are more strongly restricted in the transverse direction leading to a less efficient build-up of radiation. The importance of the transverse phase matching, which has been also emphasized in previous work [45,46], is also apparent in the regions where the coherent build-up for the two distributions is inefficient.

The results may contribute to enhance our understanding of how an efficient coherent build-up of macroscopic high harmonic generation can be achieved for different spatial focal phase distributions. The basic differences between a short Gaussian pulse and the commonly-assumed Gouy phase distribution have marked impact on the strength and cleanness of the harmonic lines as a function of the position of the gas jet in the laser focus. The conclusions drawn from the present results – for example the stronger restriction in transverse phase matching for the short Gaussian pulse phase distribution – are kept quite general, in view of the fact that the present approach includes significant approximations and certain effects have been neglected. At the present level of approximations the conclusions are qualitative only and await confirmation in experiment. In the future it will be important to analyze the impact of free electron dispersion or fluctuations of laser intensity and phase or in the gas jet density along with the short Gaussian pulse phase distribution. While we do not expect that such effects impact our general conclusions, inclusion of these and other effects in a more advanced theoretical approach are necessary towards more quantitative predictions concerning phase matching in high harmonic generation for a short Gaussian pulse phase distribution. Controlling the features of the generated radiation is important for the challenging task to design HHG sources for their effective use in spectroscopic and other applications. The present results may be relevant not only for the simulation of macroscopic high harmonic generation in atoms and molecules [3,41,47–51] but also for theoretical investigations of macroscopic propagation effects concerning high harmonic generation in solids [52–54].

Disclosures. The authors declare no conflicts of interest.

Data availability. Data underlying the results presented in this paper are not publicly available at this time but may be obtained from the authors upon reasonable request.

References

1. A. McPherson, G. Gibson, H. Jara, U. Johann, T. S. Luk, I. A. McIntyre, K. Boyer, and C. K. Rhodes, "Studies of multiphoton production of vacuum-ultraviolet radiation in the rare gases," J. Opt. Soc. Am. B **4**(4), 595–601 (1987).
2. M. Ferray, A. L'Huillier, X. F. Li, L. A. Lompre, G. Mainfray, and C. Manus, "Multiple-harmonic conversion of 1064 nm radiation in rare gases," J. Phys. B: At., Mol. Opt. Phys. **21**(3), L31–L35 (1988).
3. M. B. Gaarde, J. L. Tate, and K. J. Schafer, "Macroscopic aspects of attosecond pulse generation," J. Phys. B: At., Mol. Opt. Phys. **41**(13), 132001 (2008).
4. F. Krausz and M. Ivanov, "Attosecond physics," Rev. Mod. Phys. **81**(1), 163–234 (2009).
5. T. Popmintchev, M.-C. Chen, P. Arpin, M. M. Murnane, and H. C. Kapteyn, "The attosecond nonlinear optics of bright coherent X-ray generation," Nat. Photonics **4**(12), 822–832 (2010).
6. L. Hareli, G. Shoulga, and A. Bahabad, "Phase matching and quasi-phase matching of high-order harmonic generation—a tutorial," J. Phys. B: At., Mol. Opt. Phys. **53**(23), 233001 (2020).
7. D. Popmintchev, C. Hernández-García, F. Dollar, C. Mancuso, J. A. Pérez-Hernández, M.-C. Chen, A. Hankla, X. Gao, B. Shim, A. L. Gaeta, M. Tarazkar, D. A. Romanov, R. J. Levis, J. A. Gaffney, M. Foord, S. B. Libby, A. Jaron-Becker, A. Becker, L. Plaja, M. M. Murnane, H. C. Kapteyn, and T. Popmintchev, "Ultraviolet surprise: Efficient soft x-ray high-harmonic generation in multiply ionized plasmas," Science **350**(6265), 1225–1231 (2015).
8. T. Popmintchev, M.-C. Chen, D. Popmintchev, P. Arpin, S. Brown, S. Ališauskas, G. Andriukaitis, T. Balciunas, O. D. Mücke, A. Pugzlys, A. Baltuška, B. Shim, S. E. Schrauth, A. Gaeta, C. Hernández-García, L. Plaja, A. Becker, A. Jaron-Becker, M. M. Murnane, and H. C. Kapteyn, "Bright Coherent Ultrahigh Harmonics in the keV X-ray Regime from Mid-Infrared Femtosecond Lasers," Science **336**(6086), 1287–1291 (2012).

9. H. Eichmann, A. Egbert, S. Nolte, C. Momma, B. Wellegehausen, W. Becker, S. Long, and J. K. McIver, "Polarization-dependent high-order two-color mixing," Phys. Rev. A **51**(5), R3414–R3417 (1995).

10. A. Fleischer, O. Kfir, T. Diskin, P. Sidorenko, and O. Cohen, "Spin angular momentum and tunable polarization in high-harmonic generation," Nat. Photonics **8**(7), 543–549 (2014).

11. P.-C. Huang, C. Hernández-García, J.-T. Huang, P.-Y. Huang, C.-H. Lu, L. Rego, D. D. Hickstein, J. L. Ellis, A. Jaron-Becker, A. Becker, S.-D. Yang, C. G. Durfee, L. Plaja, H. C. Kapteyn, M. M. Murnane, A. H. Kung, and M.-C. Chen, "Polarization control of isolated high-harmonic pulses," Nat. Photonics **12**(6), 349–354 (2018).

12. L. Rego, K. M. Dorney, N. J. Brooks, Q. L. Nguyen, C.-T. Liao, J. S. Román, D. E. Couch, A. Liu, E. Pisanty, M. Lewenstein, L. Plaja, H. C. Kapteyn, M. M. Murnane, and C. Hernández-García, "Generation of extreme-ultraviolet beams with time-varying orbital angular momentum," Science **364**(6447), eaaw9486 (2019).

13. K. M. Dorney, L. Rego, N. J. Brooks, J. San Román, C.-T. Liao, J. L. Ellis, D. Zusin, C. Gentry, Q. L. Nguyen, J. M. Shaw, A. Picón, L. Plaja, H. C. Kapteyn, M. M. Murnane, and C. Hernández-García, "Controlling the polarization and vortex charge of attosecond high-harmonic beams via simultaneous spin–orbit momentum conservation," Nat. Photonics **13**(2), 123–130 (2019).

14. M. Chini, K. Zhao, and Z. Chang, "The generation, characterization and applications of broadband isolated attosecond pulses," Nat. Photonics **8**(3), 178–186 (2014).

15. A. Palacios, J. L. Sanz-Vicario, and F. Martín, "Theoretical methods for attosecond electron and nuclear dynamics: applications to the H_2 molecule," J. Phys. B: At., Mol. Opt. Phys. **48**(24), 242001 (2015).

16. M. Reduzzi, P. Carpeggiani, S. Kühn, F. Calegari, M. Nisoli, S. Stagira, C. Vozzi, P. Dombi, S. Kahaly, P. Tzallas, D. Charalambidis, K. Varju, K. Osvay, and G. Sansone, "Advances in high-order harmonic generation sources for time-resolved investigations," J. Electron Spectrosc. Relat. Phenom. **204**, 257–268 (2015).

17. J. P. Marangos, "Development of high harmonic generation spectroscopy of organic molecules and biomolecules," J. Phys. B: At., Mol. Opt. Phys. **49**(13), 132001 (2016).

18. J. Xu, C. I. Blaga, P. Agostini, and L. F. DiMauro, "Time-resolved molecular imaging," J. Phys. B: At., Mol. Opt. Phys. **49**(11), 112001 (2016).

19. M. Wu, S. Chen, S. Camp, K. J. Schafer, and M. B. Gaarde, "Theory of strong-field attosecond transient absorption," J. Phys. B: At., Mol. Opt. Phys. **49**(6), 062003 (2016).

20. F. Calegari, G. Sansone, S. Stagira, C. Vozzi, and M. Nisoli, "Advances in attosecond science," J. Phys. B: At., Mol. Opt. Phys. **49**(6), 062001 (2016).

21. H. Yun, S. J. Yun, G. H. Lee, and C. H. Nam, "High-harmonic spectroscopy of aligned molecules," J. Phys. B: At., Mol. Opt. Phys. **50**(2), 022001 (2017).

22. G. Vampa and T. Brabec, "Merge of high harmonic generation from gases and solids and its implications for attosecond science," J. Phys. B: At., Mol. Opt. Phys. **50**(8), 083001 (2017).

23. M. Nisoli, P. Decleva, F. Calegari, A. Palacios, and F. Martín, "Attosecond Electron Dynamics in Molecules," Chem. Rev. **117**(16), 10760–10825 (2017).

24. M. F. Ciappina, J. A. Pérez-Hernández, A. S. Landsman, W. A. Okell, S. Zherebtsov, B. Förg, J. Schötz, L. Seiffert, T. Fennel, T. Shaaran, T. Zimmermann, A. Chacón, R. Guichard, A. Zaïr, J. W. G. Tisch, J. P. Marangos, T. Witting, A. Braun, S. A. Maier, L. Roso, M. Krüger, P. Hommelhoff, M. F. Kling, F. Krausz, and M. Lewenstein, "Attosecond physics at the nanoscale," Rep. Prog. Phys. **80**(5), 054401 (2017).

25. R. Geneaux, H. J. B. Marroux, A. Guggenmos, D. M. Neumark, and S. R. Leone, "Transient absorption spectroscopy using high harmonic generation: a review of ultrafast X-ray dynamics in molecules and solids," Phil. Trans. R. Soc. A. **377**(2145), 20170463 (2019).

26. P. Peng, C. Marceau, and D. M. Villeneuve, "Attosecond imaging of molecules using high harmonic spectroscopy," Nat. Rev. Phys. **1**(2), 144–155 (2019).

27. A. Palacios and F. Martín, "The quantum chemistry of attosecond molecular science," WIREs Comput. Mol. Sci. **10**(1), e1430 (2020).

28. X. Shi, C.-T. Liao, Z. Tao, E. Cating-Subramanian, M. M. Murnane, C. Hernández-García, and H. C. Kapteyn, "Attosecond light science and its application for probing quantum materials," J. Phys. B: At., Mol. Opt. Phys. **53**(18), 184008 (2020).

29. B. Buades, A. Picón, E. Berger, I. León, N. Di Palo, S. L. Cousin, C. Cocchi, E. Pellegrin, J. H. Martin, S. Mañas-Valero, E. Coronado, T. Danz, C. Draxl, M. Uemoto, K. Yabana, M. Schultze, S. Wall, M. Zürch, and J. Biegert, "Attosecond state-resolved carrier motion in quantum materials probed by soft x-ray XANES," Appl. Phys. Rev. **8**(1), 011408 (2021).

30. J. L. Krause, K. J. Schafer, and K. C. Kulander, "High-order harmonic generation from atoms and ions in the high intensity regime," Phys. Rev. Lett. **68**(24), 3535–3538 (1992).

31. P. B. Corkum, "Plasma perspective on strong field multiphoton ionization," Phys. Rev. Lett. **71**(13), 1994–1997 (1993).

32. M. Lewenstein, P. Balcou, M. Y. Ivanov, A. L'Huillier, and P. B. Corkum, "Theory of high-harmonic generation by low-frequency laser fields," Phys. Rev. A **49**(3), 2117–2132 (1994).

33. A. L'Huillier, K. J. Schafer, and K. C. Kulander, "Higher-order harmonic generation in xenon at 1064 nm: The role of phase matching," Phys. Rev. Lett. **66**(17), 2200–2203 (1991).

34. P. Saliéres, A. L'Huillier, and M. Lewenstein, "Coherence Control of High-Order Harmonics," Phys. Rev. Lett. **74**(19), 3776–3779 (1995).

35. L. Gouy, "Sur une propriété nouvelle des ondes lumineuses," Compt. Redue Acad. Sci. **110**, 1251–1253 (1890).

36. M. A. Porras, "Characterization of the electric field of focused pulsed Gaussian beams for phase-sensitive interactions with matter," Opt. Lett. **34**(10), 1546–1548 (2009).

37. M. A. Porras, Z. L. Horváth, and B. Major, "Three-dimensional carrier-envelope-phase map of focused few-cycle pulsed Gaussian beams," Phys. Rev. A **98**(6), 063819 (2018).

38. D. Hoff, M. Krüger, L. Maisenbacher, A. M. Sayler, G. G. Paulus, and P. Hommelhoff, "Tracing the phase of focused broadband laser pulses," Nat. Phys. **13**(10), 947–951 (2017).

39. Y. Zhang, D. Zille, D. Hoff, P. Wustelt, D. Würzler, M. Möller, A. Sayler, and G. G. Paulus, "Observing the Importance of the Phase-Volume Effect for Few-Cycle Light-Matter Interactions," Phys. Rev. Lett. **124**(13), 133202 (2020).

40. R. Reiff, J. Venzke, A. Jaron-Becker, and A. Becker, "Interference effects in harmonic generation induced by focal phase distribution," OSA Continuum **4**(7), 1897–1906 (2021).

41. C. Hernández-García, J. A. Pérez-Hernández, J. Ramos, E. C. Jarque, L. Roso, and L. Plaja, "High-order harmonic propagation in gases within the discrete dipole approximation," Phys. Rev. A **82**(3), 033432 (2010).

42. R. Reiff, "Atomic Characteristics And High-Order Harmonic Spectra: Extension Of Ab-Initio Numerical Calculations To Larger Systems," PhD Thesis (University of Colorado Boulder, 2021).

43. E. Lorin, S. Chelkowski, and A. Bandrauk, "A numerical Maxwell–Schrödinger model for intense laser–matter interaction and propagation," Comput. Phys. Commun. **177**(12), 908–932 (2007).

44. V. V. Strelkov, V. T. Platonenko, A. F. Sterzhantov, and M. Y. Ryabikin, "Attosecond electromagnetic pulses: generation, measurement, and application. Generation of high-order harmonics of an intense laser field for attosecond pulse production," Phys.-Usp. **59**(5), 425–445 (2016).

45. C. Hernández-García, I. J. Sola, and L. Plaja, "Signature of the transversal coherence length in high-order harmonic generation," Phys. Rev. A **88**(4), 043848 (2013).

46. F. Catoire, A. Ferré, O. Hort, A. Dubrouil, L. Quintard, D. Descamps, S. Petit, F. Burgy, E. Mével, Y. Mairesse, and E. Constant, "Complex structure of spatially resolved high-order-harmonic spectra," Phys. Rev. A **94**(6), 063401 (2016).

47. C. Jin, A.-T. Le, and C. D. Lin, "Medium propagation effects in high-order harmonic generation of Ar and N_2^+," Phys. Rev. A **83**(2), 023411 (2011).

48. P.-C. Li and S.-I. Chu, "High-order-harmonic generation of Ar atoms in intense ultrashort laser fields: An all-electron time-dependent density-functional approach including macroscopic propagation effects," Phys. Rev. A **88**(5), 053415 (2013).

49. M. B. Gaarde and K. J. Schafer, "Understanding attosecond pulse generation beyond the single-atom level," J. Phys. B: At., Mol. Opt. Phys. **49**(21), 210501 (2016).

50. M. Blanco, C. Hernández-García, A. Chacón, M. Lewenstein, M. T. Flores-Arias, and L. Plaja, "Phase matching effects in high harmonic generation at the nanometer scale," Opt. Express **25**(13), 14974–14985 (2017).

51. C. Q. Abadie, M. Wu, and M. B. Gaarde, "Spatiotemporal filtering of high harmonics in solids," Opt. Lett. **43**(21), 5339–5342 (2018).

52. I. Floss, C. Lemell, G. Wachter, V. Smejkal, S. A. Sato, X.-M. Tong, K. Yabana, and J. Burgdörfer, "Ab initio multiscale simulation of high-order harmonic generation in solids," Phys. Rev. A **97**(1), 011401 (2018).

53. G. Orlando, T.-S. Ho, and S.-I. Chu, "Macroscopic effects on high-order harmonic generation in disordered semiconductors," J. Opt. Soc. Am. B **36**(7), 1873–1882 (2019).

54. I. Kilen, M. Kolesik, J. Hader, J. V. Moloney, U. Huttner, M. K. Hagen, and S. W. Koch, "Propagation Induced Dephasing in Semiconductor High-Harmonic Generation," Phys. Rev. Lett. **125**(8), 083901 (2020).